Applied Radiation and Isotopes 69 (2011) 880–889

Contents lists available at ScienceDirect

Applied Radiation and Isotopes

journal homepage: www.elsevier.com/locate/apradiso

Reconstruction of the activity of point sources for the accurate characterization of nuclear waste drums by segmented gamma scanning

Thomas Krings, Eric Mauerhofer *

Institute of Energy and Climate Research - Nuclear Waste Management, Forschungszentrum Jülich GmbH, 52425 Jülich, Germany

ARTICLE INFO

Article history:
Received 22 November 2010
Received in revised form
7 February 2011
Accepted 7 February 2011
Available online 12 February 2011

Keywords:
Collimated detector response
Segmented gamma scanning
Radioactive waste
Angular dependent count rate distribution

ABSTRACT

This work improves the reliability and accuracy in the reconstruction of the total isotope activity content in heterogeneous nuclear waste drums containing point sources. The method is based on χ^2-fits of the angular dependent count rate distribution measured during a drum rotation in segmented gamma scanning. A new description of the analytical calculation of the angular count rate distribution is introduced based on a more precise model of the collimated detector. The new description is validated and compared to the old description using MCNP5 simulations of angular dependent count rate distributions of Co-60 and Cs-137 point sources. It is shown that the new model describes the angular dependent count rate distribution significantly more accurate compared to the old model. Hence, the reconstruction of the activity is more accurate and the errors are considerably reduced that lead to more reliable results. Furthermore, the results are compared to the conventional reconstruction method assuming a homogeneous matrix and activity distribution.

1. Introduction

Radioactive waste must be characterized in order to verify its conformance with the national regulations for intermediate and final storage. Segmented gamma scanning (SGS) is the most widely applied non-destructive analytical technique for the characterization of radioactive waste drums. The isotope specific activity content is generally calculated assuming a homogeneous matrix and activity distribution for each measured drum segment (Filß, 1995). However, real radioactive waste drums exhibit non-uniform isotope and density distributions heavily affecting the reliability and accuracy of activities reconstruction in SGS (Dung, 1997, 1998). The presence of internal shielding structures in the waste drum contributes generally to a strong underestimation of the activity in particularly for radioactive sources emitting low energy gamma-rays independently of their spatial distribution.

In a previous work an improved method to quantify the activity of spatially concentrated gamma-emitting isotopes (point sources or hot spots) in heterogeneous waste drums with internal shielding structures has been developed (Bai et al., 2009). The activity of the isotope was determined by numerical simulations and χ^2-fits of the angular dependent count rate distribution recorded during the drum rotation in SGS using an analytical expression derived from a geometric model. From the quantification of Cs-137 and Co-60 activities in real heterogeneous waste drums it was demonstrated that the improved method enhances largely the accuracy of the reconstructed activity in comparison to the conventional method which assumes a homogeneous density and activity distribution. However, the isotope activity was estimated with a high uncertainty mainly due to the response of the collimated gamma-ray detector approximated by a pseudo-Dirac function in the applied geometric model. In this work the analytical expression of the improved method is revised for a more precise calculation of the angular dependent count rate distribution and thus of the activity by modifying the collimated detector response. Further, the new and the old collimator functions are compared by analyzing the angular dependent count rate distributions of Co-60 and Cs-137 point sources simulated with MCNP5 (Monte Carlo N-Particle Code) in different matrices. The obtained results are compared to the conventional method.

2. Geometric setup

Fig. 1 shows the geometric model of the segmented gamma scanner used for the characterization of nuclear waste at our institute. The emitted photons are detected with an n-type co-axial HPGe detector (30% relative efficiency). The active detector crystal has a diameter of 4.96 cm and a length of 5.31 cm. The detector is shielded by means of a lead cylinder with a cylindrical collimation

* Corresponding author.
E-mail address: e.mauerhofer@fz-juelich.de (E. Mauerhofer).

0969-8043/$ - see front matter © 2011 Elsevier Ltd. All rights reserved.
doi:10.1016/j.apradiso.2011.02.009

window. The collimator has a length l_{col} of 20.6 cm and a diameter of 22 cm. The collimation window has a radius r_{col} of 2 cm. The distance d_0 from the center of the nuclear waste drum to the detector surface is 74.6 cm. Each segment is scanned in 12 steps which leads to a rotation of the drum of 30° in each step.

The position of the point source can be described in cylindrical coordinates by its radius r_S, its height h and its polar angle φ. The origin of the coordinate system is defined by the intersection of the rotation axis of the drum and the symmetry axis of the detector (see Fig. 1). The angle between the point source and the detector is defined as $\varphi+\theta_n$ with $\theta_n=(n-1)\cdot 30^\circ$ and n being the current step of the discrete drum rotation. The reference axis for the determination of φ is defined by the detector orientation in step 1 (see dashed line in Fig. 1). Thus, the distance from the point source to the detector surface can be expressed by

$$d_n=\sqrt{d_x^2+d_y^2+d_z^2}, \tag{1}$$

with

$$d_x=d_0-r_S\cos(\varphi+\theta_n), \tag{2}$$

$$d_y=r_S\sin(\varphi+\theta_n), \tag{3}$$

$$d_z=h. \tag{4}$$

The average length covered by a photon emitted from the point source in the passive matrix may be given by

$$l_P=\frac{d_n}{d'_n}\cdot l'_P, \tag{5}$$

with

$$d'_n=\sqrt{d_x^2+d_y^2}, \tag{6}$$

$$l'_P=d'_n-d_W-\alpha d_0+\sqrt{(\alpha d_0)^2+(R-d_A)^2-d_0^2}, \tag{7}$$

$$\alpha=\frac{d_x}{d'_n}. \tag{8}$$

The mean pathlength of the photon in the absorber l_A is given by

$$l_A=\frac{d_n}{d'_n}\cdot l'_A, \tag{9}$$

with

$$l'_A=d_n-d_W-\alpha d_0+\sqrt{(\alpha d_0)^2+R^2-d_0^2}-l'_P. \tag{10}$$

The absorption of photons in the drum wall has a minor share in the total absorption. Therefore, the thickness of the drum wall d_W is taken as constant for all photon trajectories. The mean distance covered by the photon in the collimator is given by

$$l_C=\begin{cases}0, & d_n\le d_{col},\\ \dfrac{l_{col}\cdot d_n}{d_x}-\dfrac{r_{col}}{\sqrt{1-\left(\dfrac{d_x}{d_n}\right)^2}}, & d_n>d_{col},\end{cases} \tag{11}$$

and d_{col} calculated as

$$d_{col}=d_x\sqrt{1+\left(\frac{r_{col}}{l_{col}}\right)^2}. \tag{12}$$

All quantities used in the equations above are defined in Fig. 1.

3. Activity reconstruction

Based on the geometric setup in Fig. 1, the photon count rate T_n at step n can be calculated according to Bai et al. (2009) by

$$T_n=\varepsilon(d_0)K(d_n)\cdot I_\gamma A\cdot e^{-(\mu_P/\rho_P)\rho_P\cdot l_P}\cdot e^{-(\mu_A/\rho_A)\rho_A\cdot l_A}\cdot e^{-(\mu_W/\rho_W)\rho_W\cdot d_W}, \tag{13}$$

with

$\varepsilon(d_0)$: detector efficiency to a point source located axially at the distance d_0.
$K(d_n)$: collimator response function.
I_γ: intensity of the considered γ-energy of the point source.

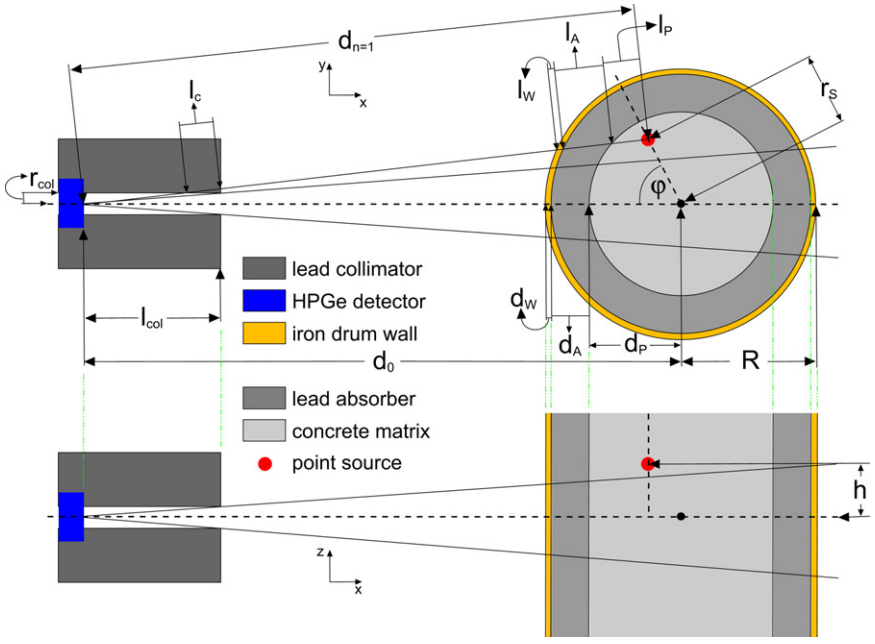

Fig. 1. Geometric model of the experimental setup used for segmented gamma scanning. The upper part shows the top view and the lower part shows the side view of the detector with a drum segment containing an activity point source.

A: activity of the point source.
μ_i: mass attenuation coefficients of the material i.
ρ_i: density of the material i.

Assuming $I_\gamma \cdot A = 1$ Bq, T_n is the detection probability for an unscattered photon emitted by a point source in 1 s counting time and is renamed to P_n. Measured photon count rates are named Z_n. Hence, the total reconstructed activity A_{reco} of a point source in the scanned segment based on the analysis of the measured angular dependent count rate distribution is given by

$$A_{reco} = \frac{\sum_{n=1}^{12} Z_n}{\sum_{n=1}^{12} P_n}. \tag{14}$$

The relative error of the reconstructed activity may be calculated by

$$\sigma_{A_{reco}} = \frac{\sqrt{n \cdot \chi^2}}{\sum_{n=1}^{12} Z_n} \cdot 100\%, \tag{15}$$

with

$$\chi^2 = \sum_{n=1}^{12} \left(\frac{P_n}{\max_n(P_n)} - \frac{Z_n}{\max_n(Z_n)} \right)^2. \tag{16}$$

Eq. (13) allows to calculate the angular dependent count rate distribution for various point source positions and different matrix configurations. By minimizing χ^2 these parameters can be fitted and used for the activity reconstruction.

4. Collimator response for a point source

The collimator response function is basically divided into two parts:

$$K(d_n) = U(d_n) + C(d_n). \tag{17}$$

Here, $U(d_n)$ describes the part of the photon beam that reaches the detector without passing the collimator material and $C(d_n)$ describes the part of the photon beam that passes some collimator material and nevertheless reaches the detector unscattered. Due to the attenuation of gamma-rays in the collimator material, $U(d_n)$ makes the major contribution to $K(d_n)$. The derivation of $U(d_n)$ requires the calculation of the solid angle that is subtended at the source by the collimator defined active detector area. Many methods have been proposed to calculate the subtended solid angle either analytically (Steyn et al., 1969; Gallagher and Cipolla, 1975; Cipolla, 2007) or by a Monte Carlo method (Nicolaou et al., 1986; Hosseini-Ashrafi and Spyrou, 1992). In this section a simple geometric algorithm for the calculation of the subtended solid angle with respect to the experimental setup shown in Fig. 1 is presented. Based on these considerations, $U(d_n)$ is defined as

$$U(d_n) = \frac{\Omega(d_n)}{\Omega(d_0)}. \tag{18}$$

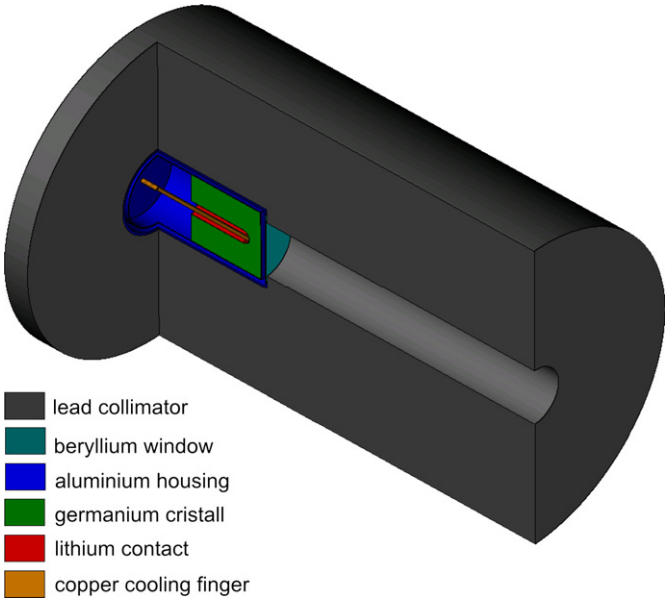

Fig. 3. Geometric implementation of the collimated n-type co-axial HPGe detector used in SGS.

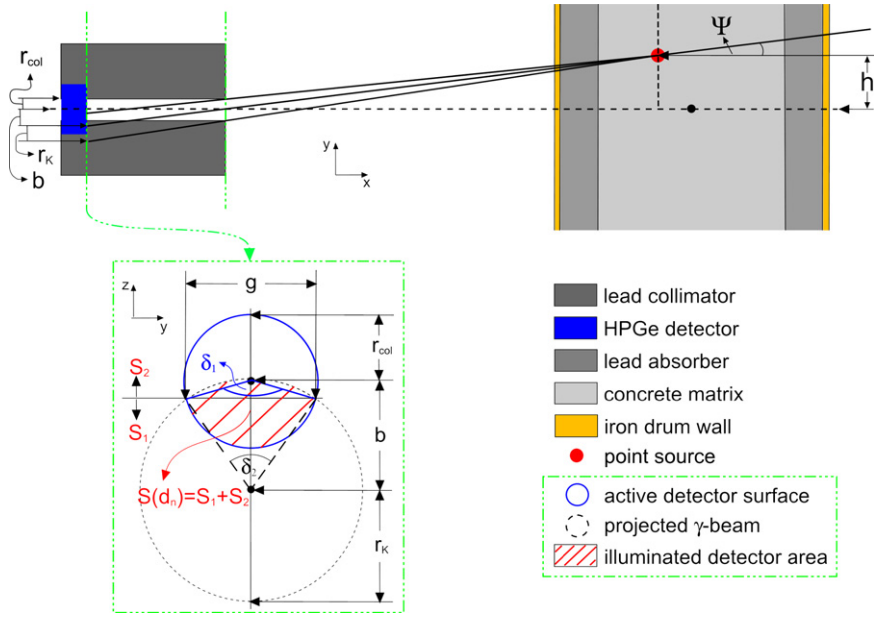

Fig. 2. Sketch of the beam geometry and active detector area illuminated with a photon beam. The diagram in the green box shows the illuminated active detector area. (For interpretation of the references to color in this figure legend, the reader is referred to the web version of this article.)

The solid angle $\Omega(d_n)$ is given by

$$\Omega(d_n) = \iint_S \frac{\vec{n}d\vec{S}}{d_n^2}, \tag{19}$$

where $\vec{n}$ is the unit vector directed from the point source at the surface element dS and d_n is the distance between the surface element and the point source. The solid angle subtended at a point source located axially at the distance d_n by the collimated detector is given by

$$\Omega(d_n) = \int_0^{2\pi}\int_0^{\theta} d\cos(\theta)\, d\varphi = 2\pi\left(1-\frac{d_n}{\sqrt{d_n^2-r_{col}^2}}\right). \tag{20}$$

Since $d_n \gg r_{col}$, this equation can be Taylor expanded in r_{col}/d_n up to the second order leading to

$$\Omega(d_n) \approx \frac{S_{det}}{d_n^2}. \tag{21}$$

Here, $S_{det} = \pi r_{col}^2$ is the active detector area that is defined by the collimator geometry. Assuming a point source located arbitrary in the scanned volume, see Fig. 2, one finds

$$\Omega(d_n) = \frac{S(d_n)}{d_n^2}\cdot\cos(\Psi), \tag{22}$$

$$\Omega(d_0) = \frac{S_{det}}{d_0^2}, \tag{23}$$

with Ψ being the angle between $\vec{n}$ and $d\vec{S}$ (see Eq. (19) and Fig. 2) and

$$U(d_n) = \frac{S(d_n)}{S_{det}}\cdot\frac{d_0^2}{d_n^2}\cos(\Psi). \tag{24}$$

For a point source in the scanned volume with an average distance to the detector of about ~ 70 cm, $\cos(\Psi)$ differs just within 0.5% from 1 and may therefore be neglected. As shown in Fig. 2, $S(d_n)$ is the area of the active detector surface that is illuminated with the photon beam because of the collimation. Due to the cylindrical symmetry of the collimator, the projection of the beam cone on the plane defined by the detector surface can always be written as

$$y^2+(z-b)^2 \le r_K^2, \tag{25}$$

with

$$b = \frac{l_{col}}{d_x-l_{col}}\cdot\sqrt{d_y^2+d_z^2}, \tag{26}$$

$$r_K = \frac{d_n}{d_n-l_{col}}\cdot r_{col}. \tag{27}$$

The active detector surface is given by

$$y^2+z^2 \le r_{col}^2. \tag{28}$$

The overlap of these two surfaces represented by the dashed red area in Fig. 2 is the illuminated active detector surface $S(d_n)$. Further, one has to distinguish three different cases:

- *Case* 1: full overlap, $S(d_n) = \pi r_{col}^2$ if
$$b \le r_K - r_{col}, \tag{29}$$
- *Case* 2: partial overlap, $0 < S(d_n) < \pi r_{col}^2$ if
$$r_K - r_{col} < b < r_K + r_{col}, \tag{30}$$
- *Case* 3: no overlap, $S(d_n)=0$ if
$$b \ge r_K + r_{col}. \tag{31}$$

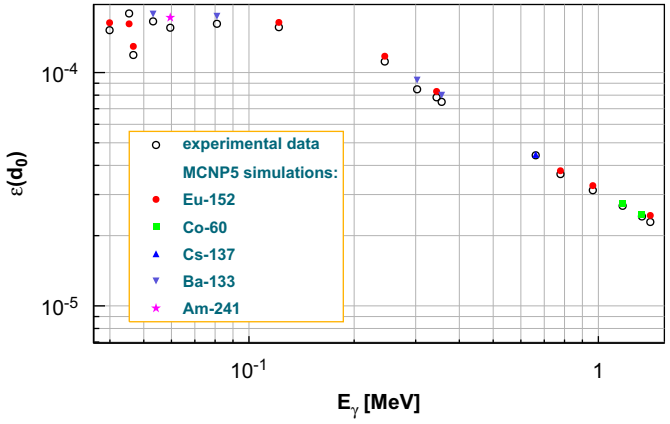

Fig. 4. Photopeak efficiencies of the detector for a point source located at d_0=74.6 cm from the detector surface. Statistical errorbars are included but in most cases they are smaller than the size of the symbols.

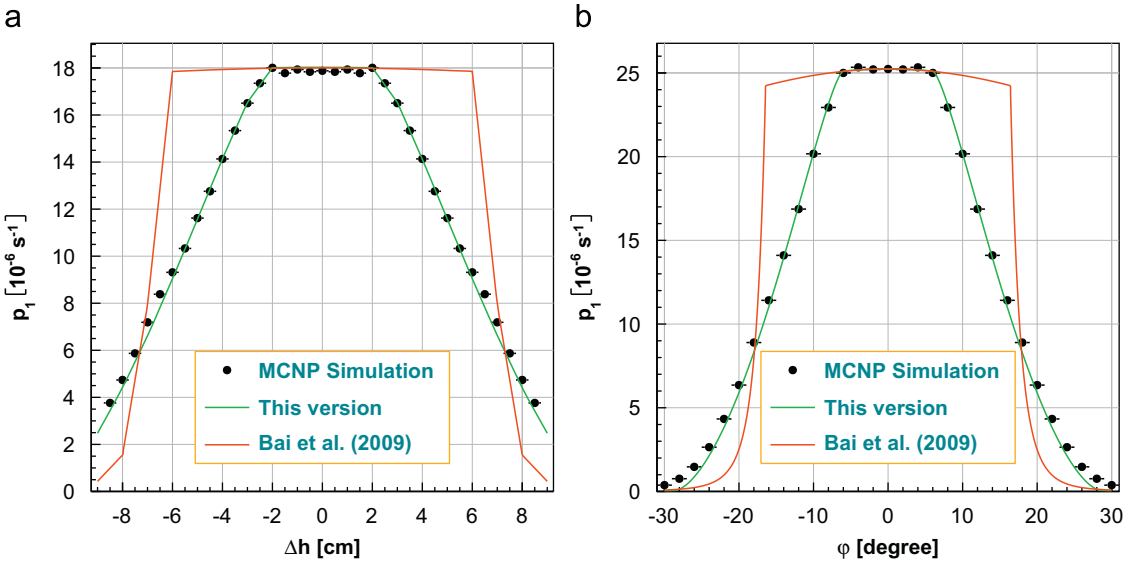

Fig. 5. Comparison of the count rates obtained for the old and new collimator model for a source (r_S=10 cm) at different heights (a) and at different polar angles (b) measured for a detector at step n=1. (For interpretation of the references to color in this figure legend, the reader is referred to the web version of this article.)

Since the calculation of the collimator response function is trivial for cases 1 and 3, the focus lies on the calculation of $S(d_n)$ in case 2. As shown in Fig. 2, $S(d_n)$ can be rewritten as (S_1+S_2), where S_1 is the circular segment which is spanned by the detector and S_2 is the circular segment spanned by the beam projection. According to geometric calculations, the areas of both circular segments are given by

$$S_1 = \frac{r_{col}^2 \cdot \delta_1}{2} - \frac{g}{2}\cos\left(\frac{\delta_1}{2}\right) r_{col}, \tag{32}$$

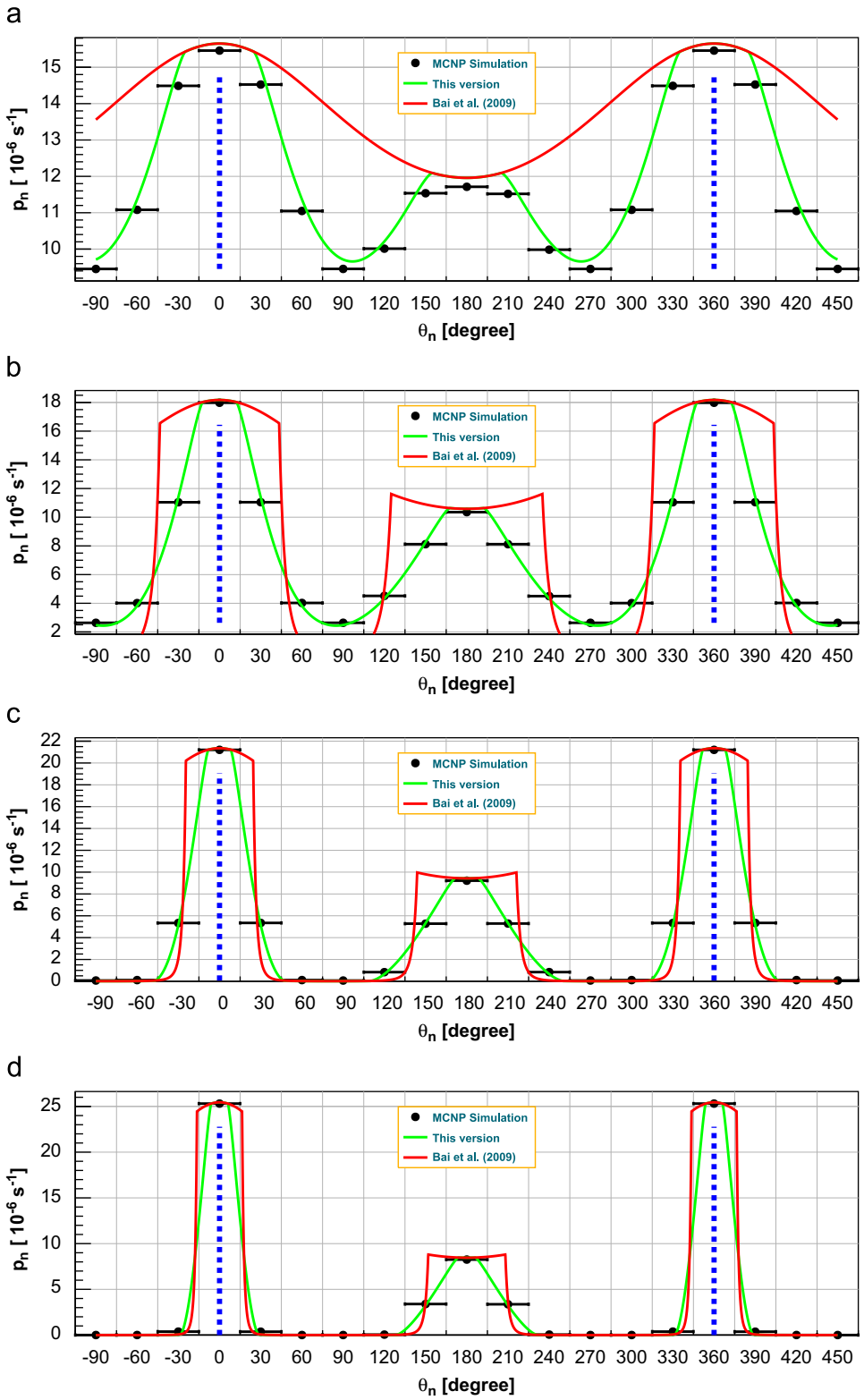

Fig. 6. Angular count rate distribution normalized per incident particle of a Co-60 point source in air ($E_\gamma = 1.1725$ MeV) at various radial positions. (a) r_S=5 cm, (b) r_S=10 cm, (c) r_S=15 cm, (d) r_S=20 cm.

$$S_2 = \begin{cases} \pi r_{col}^2 - \overline{S}_2, & b \le \cos\left(\frac{\delta_2}{2}\right) r_K, \\ \overline{S}_2, & \text{else}, \end{cases} \tag{33}$$

with

$$\overline{S}_2 = \frac{r_K^2 \cdot \delta_2}{2} - \frac{g}{2}\cos\left(\frac{\delta_2}{2}\right) r_K, \tag{34}$$

$$\delta_1 = 2 \cdot \arcsin\left(\frac{g}{2r_{col}}\right), \tag{35}$$

$$\delta_2 = 2 \cdot \arcsin\left(\frac{g}{2r_K}\right). \tag{36}$$

The length of the chord g defined by the intersections of the boundaries of the areas defined by Eqs. (25) and (28) is

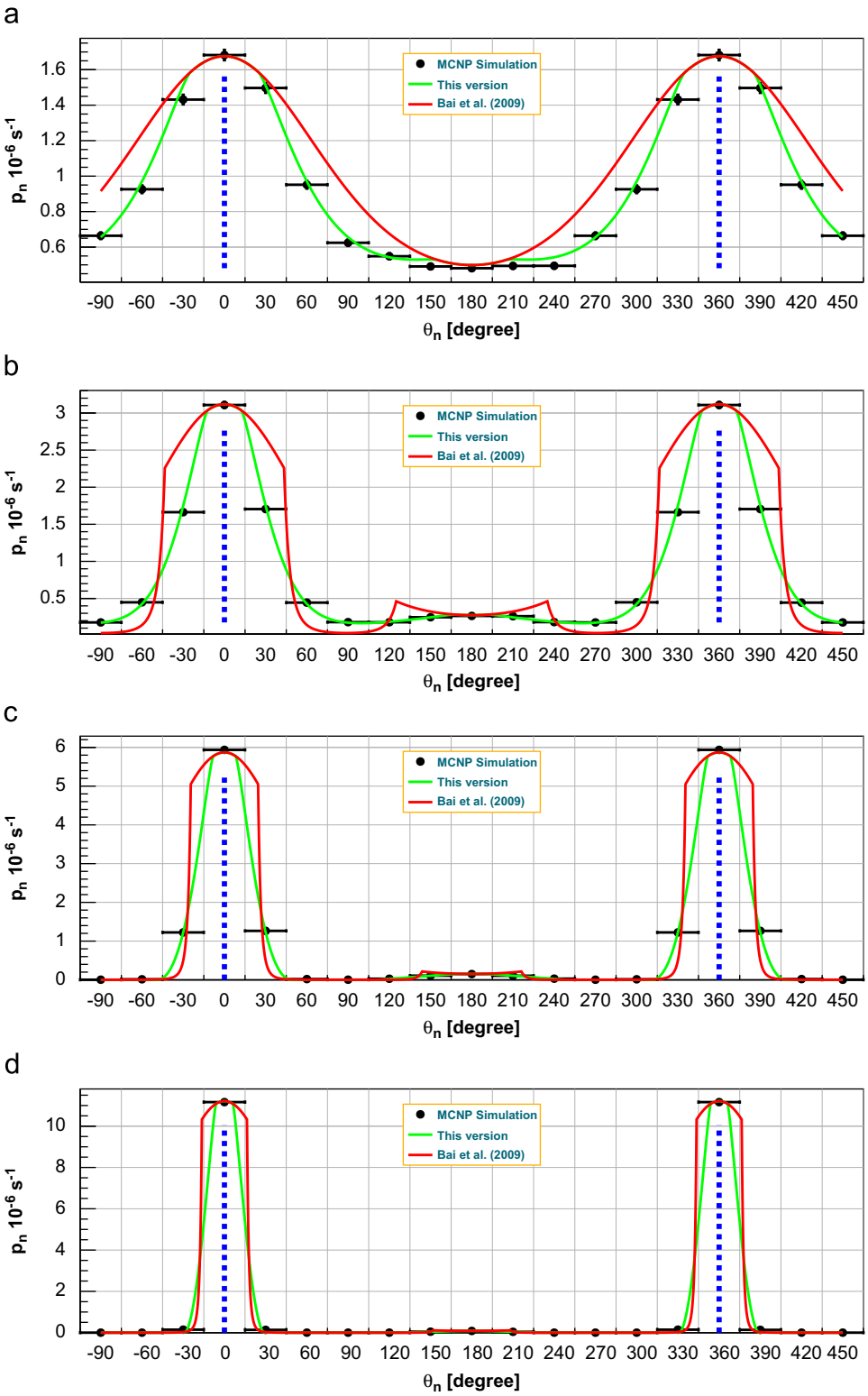

Fig. 7. Angular count rate distribution normalized per incident particle of a Co-60 point source in a concrete filled drum segment ($E_\gamma^1 = 1.1725$ MeV) at various radial positions. (a) r_S=5 cm, (b) r_S=10 cm, (c) r_S=15 cm, (d) r_S=20 cm.

given by

$$g=\sqrt{4r_K^2-\frac{(r_{col}^2-r_K^2-b^2)^2}{b^2}}. \tag{37}$$

Finally, $U(d_n)$ may be expressed in closed form:

$$U(d_n)=\frac{d_0^2}{d_n^2}\times\begin{cases}1, & b\le r_K-r_{col},\\ \dfrac{S_1+S_2}{S_{det}}, & r_K-r_{col}<b<r_K+r_{col},\\ 0, & b\ge r_K+r_{col}.\end{cases} \tag{38}$$

The part below focuses on a sufficient approximation on $C(d_n)$. The transmission probability for 1 MeV photons passing 5 cm of lead is less than 5%. Therefore, photon count rate corrections originating from point sources that only partially illuminate the active detector area do not strongly influence the activity reconstruction and may thus be computed in a simple way. The so-called edge penetration in collimated detector systems has either been studied analytically by Lee (1982) or by numerical calculations by Cook (1959). In this work, an effective penetration length l_C^{eff} is calculated and $C(d_n)$ is roughly approximated by

$$C(d_n)=(U(d_0)-U(d_n))\cdot e^{-(\mu_{col}/\rho_{col})\rho_{col}\cdot l_C^{eff}}, \tag{39}$$

with μ_{col} and ρ_{col} being the mass attenuation coefficient and the density of the collimator material, respectively. This approximation is similar to the pseudo-Dirac formulation of the collimator response function of Bai et al. (2009). The effective length is calculated according to Eqs. (11) and (12) with a redefinition of the collimator radius:

$$l_C^{eff}=\begin{cases}0, & d_n\le d_{col}^{eff},\\ \dfrac{l_{col}\cdot d_n}{d_x}-\dfrac{r_{col}^{eff}}{\sqrt{1-\left(\dfrac{d_x}{d_n}\right)^2}}, & d_n>d_{col}^{eff}.\end{cases} \tag{40}$$

The new effective collimator radius r_{col}^{eff} is calculated as

$$r_{col}^{eff}=\tfrac{1}{2}(b-r_K+r_{col}), \tag{41}$$

Table 1
Results from the reconstruction of the activity and point source position in the old and new analytical models for a 1 GBq Co-60 source ($E_\gamma=1.173$ MeV). B means biased reconstruction; the source Position given here is the input for the MCNP5 simulation. F means fitted reconstruction. C means the conventional reconstruction.

	New model							Old model						
	r_S (cm)	h (cm)	φ (deg)	χ^2 (10^{-3})	A (GBq)	σ_A (%)	$\lvert\Delta A/A\rvert$ (%)	r_S (cm)	h (cm)	φ (deg)	χ^2 (10^{-3})	A (GBq)	σ_A (%)	$\lvert\Delta A/A\rvert$ (%)
Air														
B	5	0	0	1.72	0.974	1.58	2.59	5	0	0	280	0.854	20.2	14.6
F	5	1	0	0.163	0.987	0.488	1.29	8	0	8	128	0.855	13.6	14.5
C												0.337		66.3
B	10	0	0	1.24	0.996	2.46	0.4	10	0	0	352	0.902	41.5	9.85
F	10	0.5	0	1.23	0.999	2.45	0.0808	13	1.5	0	266	0.904	36.1	9.59
C												0.214		78.6
B	15	0	0	0.488	1.01	3.02	1.12	15	0	0	138	0.98	50.8	1.98
F	15	0	0	0.488	1.01	3.02	1.12	16	1	−5	96.3	0.98	42.4	1.98
C												0.129		87.1
B	20	0	0	0.459	1.02	4.56	1.71	20	0	0	0.691	0.992	5.59	0.843
F	20	0	0	0.459	1.02	4.56	1.71	20	1.25	0	0.348	0.992	3.97	0.843
C												0.0989		90.1
B	8	1	5	26.4	1.02	8.41	1.76	8	1	5	719	0.739	43.9	26.1
F	8	0	5	3.67	1	3.14	0.16	9	1	6	326	0.728	29.6	27.2
C												0.267		73.3
B	12	2	8	109	1.07	29	6.61	12	2	8	631	0.809	69.6	19.1
F	12	0	8	4.66	0.991	5.98	0.854	13	2	1	119	0.932	30.3	6.81
C												0.171		82.9
Concrete														
B	5	0	0	6.31	0.971	4.5	2.92	5	0	0	146	0.856	21.7	14.4
F	5	1.5	−1	1.71	1	2.35	0.13	7	0	−1	54.1	0.857	13.2	14.3
C												0.0247		97.5
B	10	0	0	1	0.989	3.85	1.1	10	0	0	220	0.873	57	12.7
F	10	1.25	0	0.472	1.01	2.64	0.954	13	1.5	0	56.6	0.881	28.9	11.9
C												0.0213		97.9
B	15	0	0	0.0407	1.02	1.48	1.71	15	0	0	31.6	1.2	41.1	19.7
F	15	0	0	0.0407	1.02	1.48	1.71	14	1	0	1.26	1.2	8.22	19.7
C												0.0213		97.9
B	20	0	0	0.24	1.02	5.16	1.73	20	0	0	0.209	1.01	4.81	1.46
F	19	0	0	0.0475	1.14	2.29	13.9	21	1.75	8	0.162	1.14	4.24	13.8
C												0.0279		97.2
B	9	1	3	9.34	1.02	9.7	1.78	9	1	3	147	0.864	38.4	13.6
F	9	0	3	0.851	1	2.93	0.243	9	1.5	4	135	0.847	37	15.3
C												0.0223		97.8
B	4	0	10	24.1	0.976	7.59	2.38	4	0	10	99.1	0.915	15.4	8.53
F	4	1.75	7	1.3	1.01	1.76	1.28	5	0	6	36.4	0.916	9.35	8.41
C												0.0255		97.5

and d_{col}^{eff} is given by

$$d_{col}^{eff} = d_x \sqrt{1 + \left(\frac{r_{col}^{eff}}{l_{col}}\right)^2}. \quad (42)$$

5. MCNP simulations

To validate the described analytical model, various angular dependent count rate distributions are simulated with different combinations of point source positions and matrix configurations. The detector response and the photon tracking are simulated with the MCNP code (Forster and Godfrey, 1985) in its current version 5.1.50 (Booth et al., 2008). To determine photopeak efficiencies of the HPGe detector by Monte Carlo simulation, an accurate description of the detector including possible dead layers in the germanium crystal is required (Ewa et al., 2001; Hardy et al., 2002; Helmer et al., 2003, 2004; Rodenas et al., 2003; Maleka and Maucec, 2005; Huy et al., 2007). Fig. 3 shows the detector implementation of the collimated n-type co-axial HPGe detector used in SGS for the characterization of nuclear waste drums. A dead layer at the back side of the germanium crystal influencing mostly the measurements of high energy photons is set to 15 mm. The detector is supplied with an 0.5 mm thin beryllium window to its front entrance. The detector efficiencies are simulated for different radioactive point sources (Am-241, Ba-133, Cs-137, Co-60 and Eu-152) at a distance of $d_0 = 74.6$ cm to the surface of the detector. As shown in Fig. 4 the MCNP5 simulated photopeak efficiencies are in agreement with the measured photopeak efficiencies within less than 10% relative standard deviation. Thus, the modeled collimated detector as shown in Fig. 3 is convenient for MCNP5 simulations of angular dependent count rate distributions measured in SGS.

6. Results and discussions

MCNP5 is used to simulate count rate distributions as a function of the height and angular position for a Co-60 point source in air at a given radial position ($r_S = 10$ cm) and $n = 1$ to

Table 2
Results from the reconstruction of the activity and point source position in the old and new analytical models for a 1 GBq Co-60 source ($E_\gamma = 1.333$ MeV). B means biased reconstruction; the source position given here is the input for the MCNP5 simulation. F means fitted reconstruction. C means the conventional reconstruction.

	New model							Old model						
	r_S (cm)	h (cm)	φ (deg)	χ^2 (10^{-3})	A (GBq)	σ_A (%)	$\lvert\Delta A/A\rvert$ (%)	r_S (cm)	h (cm)	φ (deg)	χ^2 (10^{-3})	A (GBq)	σ_A (%)	$\lvert\Delta A/A\rvert$ (%)
Air														
B	5	0	0	1.72	0.974	1.58	2.64	5	0	0	273	0.854	19.9	14.6
F	5	1	0	0.307	0.987	0.668	1.33	8	0	−8	132	0.854	13.8	14.6
C												0.337		66.3
B	10	0	0	1.76	1	2.91	0.241	10	0	0	352	0.907	41.2	9.27
F	10	0	0	1.76	1	2.91	0.241	13	1.5	0	277	0.907	36.5	9.27
C												0.215		78.5
B	15	0	0	1.16	1.02	4.6	2.45	15	0	0	142	0.993	50.9	0.691
F	15	0	0	1.16	1.02	4.6	2.45	16	0.75	5	100	0.993	42.7	0.691
C												0.131		86.9
B	20	0	0	0.665	1.03	5.44	2.53	20	0	0	0.778	1	5.89	0.045
F	20	0	0	0.665	1.03	5.44	2.53	20	1.25	0	0.514	1	4.78	0.045
C												0.0997		90
B	8	1	5	25.3	1.02	8.31	1.63	8	1	5	726	0.738	44.5	26.2
F	8	0	5	2.75	1	2.74	0.0329	9	1	6	325	0.727	29.8	27.3
C												0.267		73.3
B	12	2	8	107	1.08	28.5	7.61	12	2	8	639	0.817	69.6	18.3
F	11	2	8	5.12	0.947	6.23	5.26	13	2	1	125	0.86	30.8	14
C												0.173		82.7
Concrete														
B	5	0	0	1.16	0.974	1.82	2.61	5	0	0	112	0.859	17.9	14.1
F	5	0	−1	0.973	0.974	1.67	2.61	6	0	0	57	0.859	12.8	14.1
C												0.0291		97.1
B	10	0	0	0.394	0.984	2.31	1.58	10	0	0	208	0.871	53.2	12.9
F	10	0.25	0	0.393	0.985	2.31	1.49	13	1.5	0	66.7	0.871	30.1	12.9
C												0.0242		97.6
B	15	0	0	0.508	1.02	5.04	1.62	15	0	0	40.1	1.19	44.7	19.2
F	15	0	0	0.508	1.02	5.04	1.62	14	0.5	0	1.64	1.19	9.07	19.2
C												0.0234		97.7
B	20	0	0	0.385	1.02	6.46	2.15	20	0	0	0.346	1.02	6.12	1.85
F	19	0	0	0.112	1.14	3.48	13.6	21	0.75	−8	0.258	1.13	5.29	13.3
C												0.0296		97
B	9	1	3	12.2	1.01	10.8	1.12	9	1	3	145	0.857	37.3	14.3
F	9	0	3	1.13	0.996	3.29	0.405	10	1.5	13	130	0.84	35.3	16
C												0.0255		97.5
B	4	0	10	18.2	0.981	6.24	1.89	4	0	10	61.7	0.919	11.5	8.09
F	4	0.25	9	2.06	0.984	2.1	1.65	5	2	8	29	0.919	7.86	8.09
C												0.0302		97

validate Eq. (13). The simulated and per incident particle normalized count rates can be compared to the analytically calculated count rate distributions derived in this work (new) and derived in the previous work of Bai et al. (2009) (old). The results for various heights are shown in Fig. 5(a) and for various angular positions in Fig. 5(b), respectively. In both cases the pseudo-Dirac formulation leads to a strong overestimation of the count rates up to a factor of about 2 when the source partially illuminates the active detector surface. In contrast, the count rates based on the new model (green line in Fig. 5) are in excellent agreement with the simulated ones. The small discrepancies between the new analytical count rate calculation and the simulation for increasing source displacements are due to edge penetration phenomena which are only roughly implemented in the new analytical model.

Next, MCNP5 simulations of angular count rate distributions such as measured in SGS are performed for Co-60 and Cs-137 point sources in air as well as in a segment of a drum filled with concrete ($\rho_{con} = 1.6\ \mathrm{g\ cm^{-3}}$). The 0.15 cm thick drum wall consists of stainless steel with a density of $\rho_W = 7.87\ \mathrm{g\ cm^{-3}}$. As an example, the angular dependent count rate distributions simulated for the $E_\gamma = 1.173$ MeV photons of a Co-60 point source located at various radial positions in air and in a segment of a drum filled with concrete are shown in Figs. 6 and 7, respectively.

The plots are periodically enlarged to -105° and to 465° for visualization issues. As expected, the simulated data show two maxima: one at the angular source position θ_1 and a smaller but wider one at θ_7 when the source comes again into the detector's field of view after a 180° rotation of the drum. The amplitude of the second peak at θ_7 for a point source located in a segment of the drum filled with concrete is reduced compared to the same peak in air. Besides the simulated data, the new and old calculated angular count rate distributions are shown. Generally, the angular count rate distributions calculated with the new model agree significantly better to those calculated with the old model. The discrepancy between both models decreases for increasing radial positions of the point sources. The activity reconstruction is benchmarked assuming the position of the point source and the matrix configuration are known (biased reconstruction). In a second step the position of the source is fitted according to the χ^2-procedure mentioned above under

Table 3
Results from the reconstruction of the activity and point source position in the old and new analytical models for a 1 GBq Cs-137 source ($E_\gamma = 0.662$ MeV). B means biased reconstruction; the source Position given here is the input for the MCNP5 simulation. F means fitted reconstruction. C means the conventional reconstruction.

	New model							Old model						
	r_S (cm)	h (cm)	φ (deg)	χ^2 (10^{-3})	A (GBq)	σ_A (%)	$\lvert\Delta A/A\rvert$ (%)	r_S (cm)	h (cm)	φ (deg)	χ^2 (10^{-3})	A (GBq)	σ_A (%)	$\lvert\Delta A/A\rvert$ (%)
Air														
B	5	0	0	2.33	0.976	1.85	2.38	5	0	0	296	0.856	20.8	14.4
F	5	1	0	0.191	0.989	0.529	1.08	8	0	−9	130	0.856	13.8	14.4
C												0.674		32.6
B	10	0	0	2.64	0.968	3.72	3.17	10	0	0	359	0.876	43.4	12.4
F	10	1.5	0	0.0955	0.996	0.708	0.357	13	1.5	0	222	0.897	34.1	10.3
C												0.415		58.5
B	15	0	0	0.589	0.975	3.46	2.49	15	0	0	129	0.945	51.2	5.47
F	15	1.5	0	0.0586	0.996	1.09	0.375	16	1.25	5	85.8	0.961	41.7	3.92
C												0.248		75.2
B	20	0	0	0.0155	0.999	0.855	0.134	20	0	0	0.726	0.974	5.86	2.64
F	20	0	0	0.0155	0.999	0.855	0.134	20	1.5	0	0.0135	0.974	0.801	2.64
C												0.194		80.6
B	17	0	12	354	1.04	78.9	4.02	17	0	12	597	0.918	102	8.19
F	17	0	12	0.833	0.966	3.83	3.4	16	2	8	7.46	0.747	11.4	25.3
C												0.227		77.3
B	3	1	14	5.84	1	2.45	0.236	3	1	14	17.2	0.974	4.2	2.56
F	3	0.75	14	0.237	0.997	0.493	0.302	4	2	15	10.1	0.974	3.23	2.57
C												0.764		23.6
Concrete														
B	5	0	0	2.58	0.981	3.04	1.89	5	0	0	100	0.868	18.9	13.2
F	5	0	0	2.58	0.981	3.04	1.89	6	0	0	50.7	0.868	13.5	13.2
C												0.0223		97.8
B	10	0	0	0.493	0.965	2.98	3.5	10	0	0	186	0.843	57.9	15.7
F	10	1	0	0.167	0.978	1.74	2.24	13	1.5	0	32.8	0.847	24.3	15.3
C												0.0217		97.8
B	15	0	0	0.587	0.969	6.02	3.07	15	0	0	20.6	1.15	35.6	15.2
F	15	1.75	0	0.0105	0.998	0.805	0.166	14	1.25	0	0.312	1.2	4.38	19.6
C												0.0259		97.4
B	20	0	0	0.0028	1	0.574	0.168	20	0	0	0.000633	1	0.273	0.0153
F	19	2	0	0.0021	1.17	0.497	17.2	20	0	0	0.000633	1.17	0.273	17
C												0.0419		95.8
B	13	2	6	49.2	1.04	42.6	3.66	13	2	6	51.1	0.928	43.5	7.19
F	13	0.5	6	0.0424	0.971	1.25	2.93	14	0	2	9.32	0.856	18.6	14.4
C												0.0236		97.6
B	7	0	7	41.4	0.989	16.9	1.12	7	0	7	289	0.754	44.8	24.6
F	7	0.75	7	0.261	0.992	1.34	0.785	8	2	5	89.8	0.754	24.9	24.6
C												0.0221		97.8

the constraint of a known matrix. Hence, the activity is reconstructed using the best fit parameter (fitted reconstruction). These results are compared with the activity reconstruction assuming a homogeneous activity and matrix distribution (conventional reconstruction). The corresponding results are summarized in Tables 1 and 2 for Co-60 and in Table 3 for Cs-137, respectively.

In comparison to the conventional method, both improved methods enhance largely the accuracy in the activity reconstruction. However, the new method employed for the calculation of the angular dependent count rate distributions leads to a more precise activity reconstruction than the old calculation method. The mean deviation from the true activity lies around 1–3% in the new model and around 10–40% in the old model depending on the source position and the matrix configuration. The improvement in the accuracy of the activity reconstruction becomes less important for point sources at increasing radial positions. Furthermore, the error of the reconstructed activity is considerably reduced leading to a high reliability. The new method allows also a better position reconstruction than the old method.

7. Conclusion

In comparison to the old model, the new model describing the angular dependent count rate distribution presented in this work provides a more accurate reconstruction of the activity and the position of a point source. Improvements of the precision in the activity and position reconstruction can be further obtained by incorporating the height dependent count rate distribution in the fitting process. Additionally, the effects of extended and multiple sources in the scanned segment have to be investigated.

Acknowledgments

The authors would like to thank S. Schneider for his valuable help during the simulation phase and for numerous helpful discussions. Furthermore, the authors would like to thank M. Rossbach for comments regarding the preparation of the manuscript.

References

Bai, Y., Mauerhofer, E., Wang, D., Odoj, R., 2009. An improved method for the non-destructive characterization of radioactive waste by gamma scanning. Applied Radiation and Isotopes 67 (10), 1897–1903.

Booth, T., et al., 2008. Mcnp5 1.50 release notes.

Cipolla, S.J., 2007. Calculating the solid angle for different source shapes and orientations as viewed by a detector with a cylindrical collimator. Nuclear Instruments and Methods in Physics Research Section A: Accelerators, Spectrometers, Detectors and Associated Equipment 579 (1), 268–271.

Cook, C.S., 1959. Calculation of the penetration of gamma rays through the edges of a 1/2-inch diameter lead collimator. Nuclear Instruments and Methods 4 (2), 103–106.

Dung, T.Q., 1997. Calculation of the systematic error and correction factors in gamma waste assay system. Annals of Nuclear Energy 24 (1), 33–47.

Dung, T.Q., 1998. Some theoretical results of gamma techniques for measuring large samples. Nuclear Instruments and Methods in Physics Research Section A: Accelerators, Spectrometers, Detectors and Associated Equipment 416 (2–3), 505–515.

Ewa, I.O.B., Bodizs, D., Czifrus, S., Molnar, Z., 2001. Monte Carlo determination of full energy peak efficiency for a HPGe detector. Applied Radiation and Isotopes 55 (1), 103–108.

Filß, P., 1995. Relation between the activity of a high-density waste drum and its gamma count rate measured with an unshielded Ge-detector. Applied Radiation and Isotopes 46 (8), 805–812.

Forster, R., Godfrey, T., 1985. MCNP - a general Monte Carlo code for neutron and photon transport. Lecture Notes in Physics, vol. 240. Springer, Berlin/Heidelberg, 10.1007/BFb0049033.

Gallagher, W.J., Cipolla, S.J., 1975. A method for accurately determining the thickness dimensions and photon-intensity corrections of a thick, covered, photon source. Nuclear Instruments and Methods 125 (2), 269–276.

Hardy, J., Iacob, V., Sanchez-Vega, M., Effinger, R., Lipnik, P., Mayes, V., Willis, D., Helmer, R., 2002. Precise efficiency calibration of an HPGe detector: source measurements and Monte Carlo calculations with sub-percent precision. Applied Radiation and Isotopes 56 (1–2), 65–69.

Helmer, R.G., Hardy, J.C., Iacob, V.E., Sanchez-Vega, M., Neilson, R.G., Nelson, J., 2003. The use of Monte Carlo calculations in the determination of a Ge detector efficiency curve. Nuclear Instruments and Methods in Physics Research Section A: Accelerators, Spectrometers, Detectors and Associated Equipment 511 (3), 360–381.

Helmer, R.G., Nica, N., Hardy, J.C., Iacob, V.E., 2004. Precise efficiency calibration of an HPGe detector up to 3.5 MeV, with measurements and Monte Carlo calculations. Applied Radiation and Isotopes 60 (2–4), 173–177.

Hosseini-Ashrafi, M., Spyrou, N., 1992. Calculation of the average solid angle subtended by a photon-emitting source at a collimated detector and the contribution of collimator edge penetration. International Journal of Radiation Applications and Instrumentation. Part A. Applied Radiation and Isotopes 43 (12), 1449–1460.

Huy, N., Binh, D., An, V., 2007. Study on the increase of inactive germanium layer in a high-purity germanium detector after a long time operation applying MCNP code. Nuclear Instruments and Methods in Physics Research Section A: Accelerators, Spectrometers, Detectors and Associated Equipment 573 (3), 384–388.

Lee, H., 1982. Edge penetration by radiation through a collimation system. Nuclear Instruments and Methods in Physics Research 197 (2–3), 411–416.

Maleka, P., Maucec, M., 2005. Monte Carlo uncertainty analysis of germanium detector response to γ-rays with energies below 1 MeV. Nuclear Instruments and Methods in Physics Research Section A: Accelerators, Spectrometers, Detectors and Associated Equipment 538 (1–3), 631–639.

Nicolaou, G.E., Khrbish, Y.S., Spyrou, N.M., 1986. The effect of solid angle on the reproducibility of an experimental set-up in prompt gamma-ray neutron activation analysis. International Journal of Radiation Applications and Instrumentation. Part A. Applied Radiation and Isotopes 37 (12), 1219–1224.

Rodenas, J., Pascual, A., Zarza, I., Serradell, V., Ortiz, J., Ballesteros, L., 2003. Analysis of the influence of germanium dead layer on detector calibration simulation for environmental radioactive samples using the Monte Carlo method. Nuclear Instruments and Methods in Physics Research Section A: Accelerators, Spectrometers, Detectors and Associated Equipment 496 (2–3), 390–399.

Steyn, J., Andrews, D., Dixmier, M., 1969. Collimated detector response to point, line and plane sources. Nuclear Instruments and Methods 74 (1), 123–131.